Charge-dependent spectral softenings of primary cosmic-rays below the knee

DAMPE Collaboration*

Abstract

In most particle acceleration or propagation theories, the characteristic features of the cosmic ray spectra due to acceleration limits or propagation phase changes are charge dependent[1–4]. Alternatively, the interaction scenario would expect mass dependent spectral features in general. The observational verification of which relation takes effect in nature is still lack due to the difficulty of measuring the spectra of individual particles up to very high energies. Here we report direct measurements of the carbon, oxygen, and iron spectra from $\sim$ 20 gigavolts to $\sim$ 100 teravolts ($\sim$ 60 teravolts for iron) with 9 years of on-orbit data collected by the Dark Matter Particle Explorer. Distinct spectral softenings have been directly detected in these spectra for the first time. Combined with the updated proton and helium spectra, the spectral softening appears universally at a rigidity of $\sim$ 15 teravolts. A nuclei mass dependent softening is rejected at a confidence level of $> 99.999\%$. Possible interpretations of these results, including a nearby cosmic ray source[5–7] and other models such as the propagation effect[8], are discussed.

* Members of DAMPE Collaboration are listed at the end of this paper.
Email: dampe@pmo.ac.cn

Cosmic rays (CRs) are energetic particles travelling through the Universe as high-energy beams. They are predominantly made up of nuclei, such as protons, heavier ions up to iron and beyond[2]. Depending on the production processes, CRs are typically divided into two classes, the primary species accelerated by sources and secondary species produced due to fragmentation of primary CRs via collisions with the interstellar medium (ISM). High abundance particles such as protons, helium, carbon, oxygen, and iron nuclei are believed to be dominated by primary origin, while lithium, beryllium, boron, and sub-iron nuclei belong to the secondary family[9]. Spectral structures of CRs are very important probes to understanding the physics of CRs such as the acceleration, propagation, and interactions. In the general picture of particle acceleration and propagation, charge-dependent spectral features are expected due to gyration of particles in the magnetic fields. On the other hand, in case of particle interactions with characteristic thresholds, the break off energy of particles would be mass dependent. Obtaining observational evidence to verify which factor shapes the CR spectra is highly challenging and remains elusive. To convincingly test this, precise spectra of individual CR species covering a wide range of charge numbers need to be measured up to very high energies, which requires sensitive detectors with large acceptance and good charge/energy resolution.

Important progresses on precise measurements of energy spectra of different mass compositions have been achieved in recent years. Direct measurements of the spectra of individual CR species by space-borne and balloon-borne experiments have revealed unexpected hardening features around a few hundred GV rigidity[10–19], deviating from the power-law (PL) expectation from the conventional theories of the acceleration and propagation of CRs. In addition, spectral softenings around $\sim 10-30$ TeV have also been revealed in the proton and helium spectra[14, 15, 18–21] (there were also hints from earlier experiments[11, 22, 23], but with relatively large statistical and systematic uncertainties). These new findings challenge the standard CR paradigm that a single source population with PL spectra accounts for the measured CR spectra below the so-called knee[24], giving new insights on the understanding of CR physics. Though also being among the most abundant species in CRs, the measurements of carbon, oxygen, and iron nuclei spectra in CRs are rather challenging, and the current precise measurements are limited to a rigidity of a few TV. Similar hardening features as lighter nuclei have been detected for carbon and oxygen nuclei[12, 25], while the iron spectrum is found to be consistent with a single PL above 100 GV[26, 27]. The high-

energy spectral behaviors of these medium and heavy nuclei are unclear yet, which hinders a critical understanding of the acceleration and propagation physics of CRs.

In this work, we report the direct measurements of the carbon, oxygen, and iron spectra up to PeV energies with the Dark Matter Particle Explorer (DAMPE)[28, 29]. DAMPE is a space-borne, calorimeter-type detector for high-energy particles and photons. With the plastic scintillator detector (PSD[30]), the silicon tungsten tracker-converter (STK[31]), the bismuth germanium oxide calorimeter (BGO[32]), and the neutron detector (NUD[33]), DAMPE is able to measure precisely the charge, direction, energy and particle identity of high-energy CRs. Particularly, the thick calorimeter (with $\sim$ 32 radiation lengths) is designed for observing CR electrons/positrons and γ rays to energies beyond 10 TeV with a very high energy resolution[29]. The relatively large geometric factor ($\sim$ 0.3 m^2 sr) and nuclear interaction depth ($\sim 1.6\lambda_0$) make it also a powerful detector of CR nuclei to hundreds of TeV energies[14, 15].

The analysis presented in this work is based on the data recorded in the first 9 years of DAMPE's on-orbit operation, from January 1, 2016 to December 31, 2024. The live time fraction is about 76.2% after excluding the instrument dead time, the time for on-orbit calibration, the time in the South Atlantic Anomaly (SAA) region, and the period between September 9, 2017 and September 13, 2017 during which a big solar flare occurred and affected the status of the detector[34]. The carbon, oxygen, and iron nuclei are efficiently identified based on the PSD charge measurements. The residual backgrounds for selected candidates are evaluated based on the template fitting for the Monte Carlo (MC) simulated charge distributions (see the Methods for details). The selection efficiency and the energy response are also obtained with MC simulations, and are validated based on the flight data and the test beam data. An unfolding procedure[35] is applied to the observed count spectrum to correct the bin-by-bin migration of events due to the limited energy resolution of the detector. The obtained energy spectra of carbon, oxygen, and iron nuclei, together with the updated proton and helium spectra, in the rigidity range from $\sim$ 20 GV to $\sim$ 100 TV (60 TV for iron) are shown in Figure 1. Compared with previous measurements of carbon, oxygen, and iron nuclei by the Alpha Magnetic Spectrometer (AMS-02[12, 26]) and the Calorimetric Electron Telescope (CALET[25, 27]), the DAMPE results improve the precision considerably at high energies and provide the first precise measurements of these spectra above several TV.

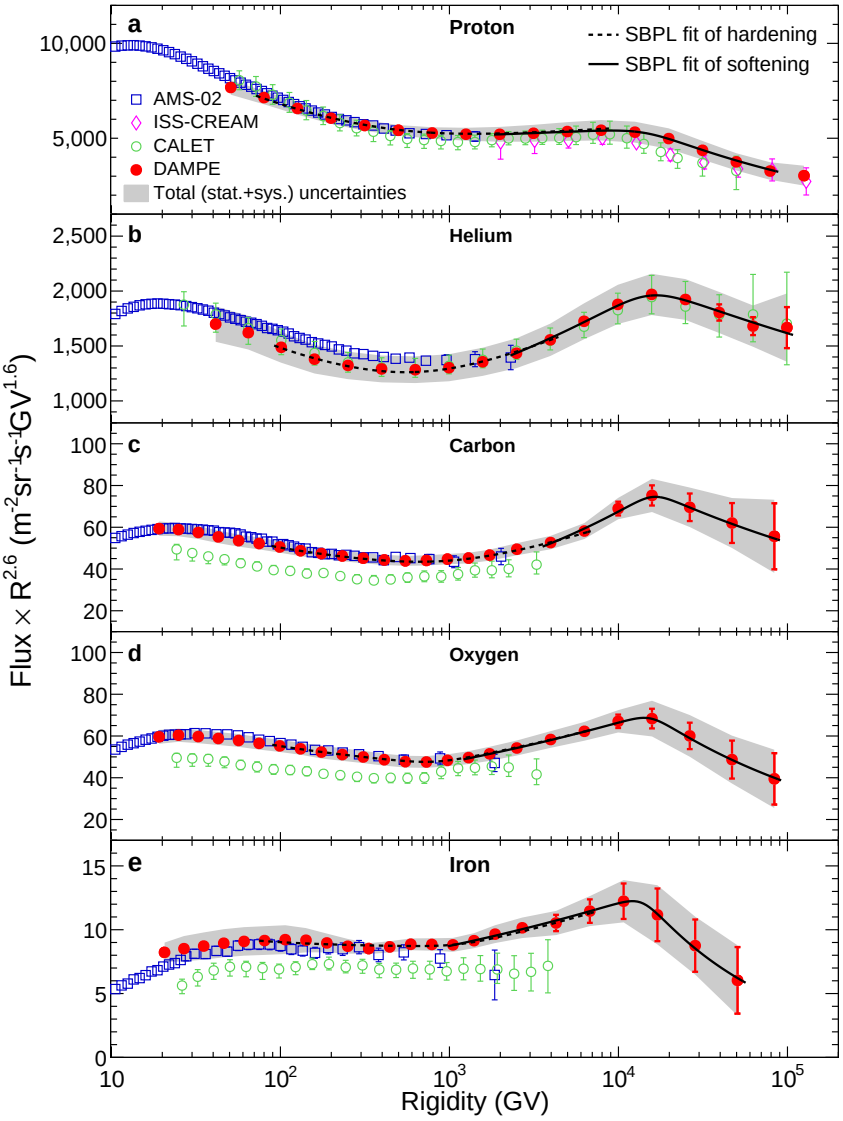

FIG. 1: **Rigidity spectra.** Panels **a** - **e** show the spectra of protons, helium, carbon, oxygen, and iron, weighted by $R^{2.6}$. Red dots are the DAMPE measurements, with $\pm 1\sigma$ statistical uncertainties (errorbars) and the total statistical and systematic uncertainties added in quadrature (shaded bands). Dashed and solid lines show the best-fitting results of the SBPL function. The fluxes are converted from the total kinetic energy bins to rigidity bins assuming a mass number of 12, 16, and 56 for carbon, oxygen, and iron. For proton and helium, the average mass number is calculated assuming D/p= 0.027 and ^{3}He/^{4}He= $0.142 \times (R/4.5\ \mathrm{GV})^{-0.289}$ based on the AMS-02 measurements[45]. Also shown are the measurements from other experiments: AMS-02[12, 13, 26], CALET[18, 19, 25, 27], and the Cosmic Ray Energetics And Mass on the International Space Station (ISS-CREAM)[21].

It can be clearly found that similar spectral structures, i.e. a hardening at $\sim 500-1000$ GV rigidity followed by a softening at ~ 15 TV, are observed among all the five species of CRs. The spectral fitting with a smoothly broken power-law (SBPL) model (see the Methods) provides significance of the hardening of 29σ, 23σ, 11σ, 10σ, and 2.7σ with hardening rigidity at 590 ± 40, 595 ± 40, 892 ± 210, 799 ± 76, and 1104 ± 435 GV for proton, helium, carbon, oxygen, and iron, respectively. The smoothness parameter of the break can also be obtained (except for iron), as given in Table S6. The results show that in general a smooth hardening is favored by the data. Although the spectra of all these CR species show similar hardening features, their detailed spectral shapes and break rigidities (energies) differ from each other. Fitting to the AMS-02[13] and CALET measurements give also diverse results of the hardening rigidities[18, 19, 25, 36]. Measurements of the secondary-to-primary ratios of CRs such as B/C and B/O show hardenings around 200 GV[13, 16, 37], which is different from the break rigidities found here for primary CRs. This may suggest that the hardenings of primary and secondary CRs are not solely due to the same origin such as a unified propagation effect[38].

What is more interesting is the spectral softening which is for the first time clearly identified in the spectra of carbon, oxygen, and iron. The significance of the softening is 3.2σ, 4.1σ and 2.4σ with the break rigidity of 16.1 ± 5.6, 15.4 ± 4.8, and 13.8 ± 6.0 TV for carbon, oxygen, and iron, respectively. The updated proton and helium spectra yield softening rigidity at 14.6 ± 1.3 and 15.3 ± 2.3 TV, respectively. It has been clearly established that the softenings occur at the same rigidity for all the five species, as shown in Figure 2. The proportional relation between the particle charge Z (for the four species with $Z \geq 2$) and the softening energy $E_{\rm br}$ is best fitted as $\bar{E}_{\rm br}/{\rm TeV} = (15.3 \pm 1.6) \times Z$, which is well consistent with the $E_{\rm br}$ of proton, i.e. 14.6 ± 1.3 TeV. Assuming a general power-law scaling of the break energy and the charge, we get the fitting power-law index of 1.01 ± 0.09, which shows a good consistency with the linear correlation. On the other hand, the mass number (A) dependence of the softening energies can be excluded at a confidence level of $> 99.999\%$ (4.4σ) by comparing the $E_{\rm br}/{\rm TeV} = 14.6 \pm 1.3$ for proton and the $\bar{E}_{\rm br}/{\rm TeV} = (7.6 \pm 0.9) \times A$ for other four species with $Z \geq 2$. The universal softening feature in the spectra of primary CRs from protons ($Z = 1$) to iron nuclei ($Z = 26$) and the charge-dependence of the softening energy indicate a common origin of the break due to acceleration or propagation effect.

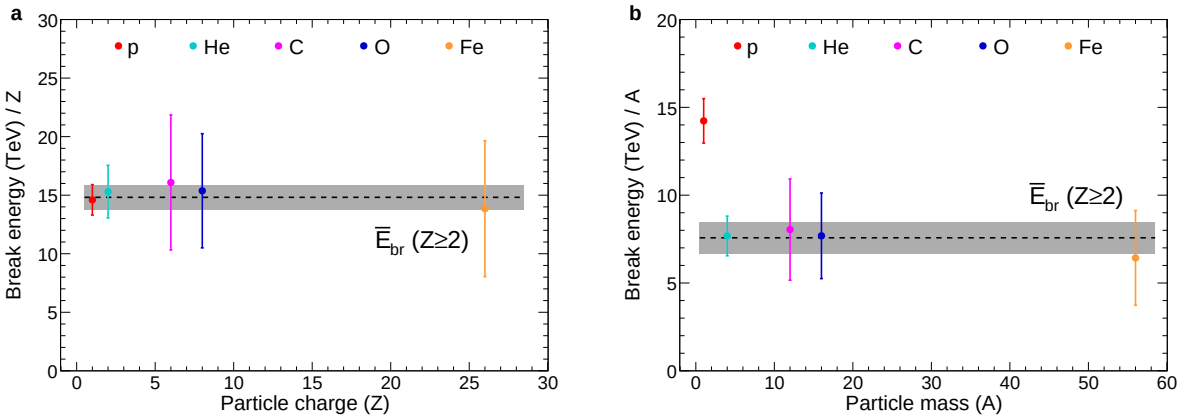

FIG. 2: **The break energy for different species.** Panel **a** shows the break energy divided by Z as a function of particle charge Z, and panel **b** is that divided by A as a function of mass number A. The average mass number A is assumed to be 1.026, 3.985, 12, 16, and 56 for proton, helium, carbon, oxygen, and iron, respectively. The shaded bands represent the average softening energies of the particles heavier than proton.

The spectra can be decomposed into two components, a soft component which dominates the CR fluxes in the low-energy band, and a hard component with a spectral cutoff which contributes mainly to the bump feature. A simple idea to account for the spectral structures is the superposition of a nearby source on top of the background source population[5–7], as shown by solid lines in Figure 3. The addition of the nearby source component with proper distance and age can simultanesouly reproduce the observed energy evolution of the amplitudes and phases of the dipole anisotropies (see Figure S4). See the Methods for details of the model setting. In this scenario, the spectrum from the nearby source shows both low-energy suppression due to the inefficient propagation of these particles within the age of the source and high-energy suppression due to the acceleration limit, and hence produces naturally a bump structure. Assuming an exponential form of the spectral cutoff, we obtain a cutoff rigidity of about 30 TV for the nearby source, which is consistent with the estimation of acceleration by supernova remnants[39]. Supposing the spectral features are indeed imprints from a nearby source, we propose that the supernova explosion associated with the Geminga pulsar could be a good candidate for this source, given its proper age, distance, and location in the sky[7, 40]. The energetics needed to account for the data is

about 3.3×10^{50} erg, which is consistent with that can be produced for a typical core collapse supernova. Via comparing the relative abundances of nuclei at $R = 0.1$ TV and $R = 10$ TV, we can infer that the metallicity of the nearby source may be slightly higher than the average value of the background source population, as shown in Figure S5.

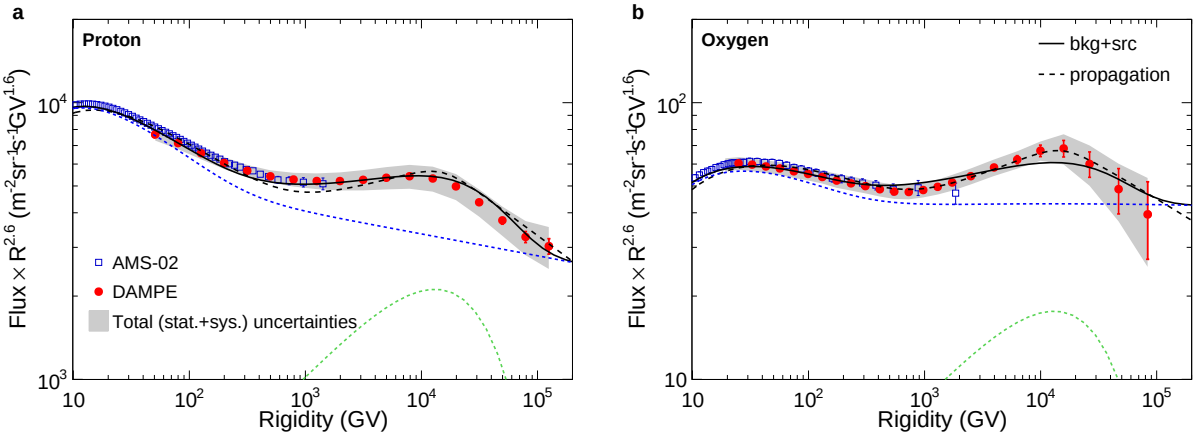

FIG. 3: **Comparison of the spectra with model expectations.** Panel **a** is for protons, and panel **b** is for oxygen nuclei. Solid lines show the model expectations of the background plus nearby source scenario, with individual contributions from the two components being shown by dotted lines (blue for the background and green for the nearby source), and dashed lines show the results of the propagation scenario.

Alternatively, the spectral breaks could be due to a propagation effect, especially that universal spectral hardenings have been found in the secondary-to-primary ratios[13, 16, 37]. The physical modeling of the effect of self-generated turbulence with nonlinear Landau and ion-neutral damping of magnetohydrodynamic waves by CRs can properly account for both the hardening and softening of the proton spectrum[8]. As an effective approach, we introduce two breaks of the diffusion coefficient to mimic the change of propagation properties, and calculate the propagated spectra. The results are shown by dashed lines in Figure 3. The detailed parameter setting can be found in the Methods. The spectral structures observed by DAMPE and AMS-02 can also be properly reproduced by this model.

Additional theoretical models to account for the bump structures include multiple source populations[41, 42], and the re-acceleration of CRs by a local star[43]. All these models can properly explain the features of the spectra. To explain the large-scale anisotropies in

these scenarios, additional assumptions about the source distribution and/or magnetic field configuration are necessary[44]. The DAMPE results reported in this work demonstrate a clear presence of rigidity-dependent softening features in the spectra of primary CR nuclei, indicating a common origin due to acceleration and/or propagation processes.

Acknowledgments: The DAMPE mission was funded by the strategic priority science and technology projects in space science of Chinese Academy of Sciences (CAS). In China, the data analysis is mainly supported by the National Natural Science Foundation of China (No. 12588101) and the National Key Research and Development Program of China (No. 2022YFF0503302). Additional supports are from the CAS Project for Young Scientists in Basic Research (Nos. YSBR-061 and YSBR-092), the NSFC (Nos. 12220101003, 12503107), the Strategic Priority Program on Space Science of CAS (No. E02212A02S), the Youth Innovation Promotion Association of CAS, the Young Elite Scientists Sponsorship Program by CAST (No. YESS20220197), the Natural Science Foundation of Jiangsu Province (No. SBK20250300783), and the Program for Innovative Talents and Entrepreneur in Jiangsu. Y.Z.F thanks the support of New Cornerstone Science Foundation through the XPLORER PRIZE. In Europe, the activities and data analysis are supported by the Swiss National Science Foundation (SNSF), Switzerland, the National Institute for Nuclear Physics (INFN), Italy, and the European Research Council (ERC) under the European Union's Horizon 2020 research and innovation programme (No. 851103), and the Swiss State Secretariat for Education, Research and Innovation (SERI).

---

[1] Peters, B. Primary cosmic radiation and extensive air showers. *Nuovo Cim.* **22**, 800–819 (1961).

[2] Hillas, A. M. The Origin of Ultrahigh-Energy Cosmic Rays. *Ann. Rev. Astron. Astrophys.* **22**, 425–444 (1984).

[3] Bell, A. R. Cosmic ray acceleration. *Astropart. Phys.* **43**, 56–70 (2013).

[4] Cesarsky, C. J. Cosmic Ray Confinement in the Galaxy. *Ann. Rev. Astron. Astrophys.* **18**, 289–319 (1980).

[5] Savchenko, V., Kachelrieß, M. & Semikoz, D. V. Imprint of a 2 Million Year old Source on the Cosmic-ray Anisotropy. *Astrophys. J. Lett.* **809**, L23 (2015). 1505.02720.

[6] Ahlers, M. Deciphering the Dipole Anisotropy of Galactic Cosmic Rays. *Phys. Rev. Lett.* **117**, 151103 (2016). 1605.06446.

[7] Liu, W., Guo, Y.-Q. & Yuan, Q. Indication of nearby source signatures of cosmic rays from energy spectra and anisotropies. *J. Cosmol. Astropart. Phys.* **10**, 010 (2019). 1812.09673.

[8] Chernyshov, D. O., Dogiel, V. A., Ivlev, A. V., Erlykin, A. D. & Kiselev, A. M. Formation of the Cosmic-Ray Halo: The Role of Nonlinear Landau Damping. *Astrophys. J.* **937**, 107 (2022). 2209.12302.

[9] Strong, A. W., Moskalenko, I. V. & Ptuskin, V. S. Cosmic-ray propagation and interactions in the Galaxy. *Ann. Rev. Nucl. Part. Sci.* **57**, 285–327 (2007). astro-ph/0701517.

[10] Adriani, O. *et al.* PAMELA Measurements of Cosmic-ray Proton and Helium Spectra. *Science* **332**, 69–72 (2011). 1103.4055.

[11] Panov, A. D. *et al.* Energy Spectra of Abundant Nuclei of Primary Cosmic Rays from the Data of ATIC-2 Experiment: Final Results. *Bull. Russ. Acad. Sci. Phys.* **73**, 564–567 (2009). 1101.3246.

[12] Aguilar, M. *et al.* Observation of the Identical Rigidity Dependence of He, C, and O Cosmic Rays at High Rigidities by the Alpha Magnetic Spectrometer on the International Space Station. *Phys. Rev. Lett.* **119**, 251101 (2017).

[13] Aguilar, M. *et al.* The Alpha Magnetic Spectrometer (AMS) on the international space station: Part II — Results from the first seven years. *Phys. Rept.* **894**, 1–116 (2021).

[14] An, Q. *et al.* Measurement of the cosmic-ray proton spectrum from 40 GeV to 100 TeV with the DAMPE satellite. *Sci. Adv.* **5**, eaax3793 (2019). 1909.12860.

[15] Alemanno, F. *et al.* Measurement of the cosmic ray helium energy spectrum from 70 GeV to 80 TeV with the DAMPE space mission. *Phys. Rev. Lett.* **126**, 201102 (2021). 2105.09073.

[16] Alemanno, F. *et al.* Detection of spectral hardenings in cosmic-ray boron-to-carbon and boron-to-oxygen flux ratios with DAMPE. *Sci. Bull.* **67**, 2162–2166 (2022). 2210.08833.

[17] Alemanno, F. *et al.* Observation of a Spectral Hardening in Cosmic Ray Boron Spectrum with the DAMPE Space Mission. *Phys. Rev. Lett.* **134**, 191001 (2025). 2412.11460.

[18] Adriani, O. *et al.* Observation of Spectral Structures in the Flux of Cosmic-Ray Protons from 50 GeV to 60 TeV with the Calorimetric Electron Telescope on the International Space Station. *Phys. Rev. Lett.* **129**, 101102 (2022). 2209.01302.

[19] Adriani, O. *et al.* Direct Measurement of the Cosmic-Ray Helium Spectrum from 40 GeV to

250 TeV with the Calorimetric Electron Telescope on the International Space Station. *Phys. Rev. Lett.* **130**, 171002 (2023). 2304.14699.

[20] Atkin, E. *et al.* New Universal Cosmic-Ray Knee near a Magnetic Rigidity of 10 TV with the NUCLEON Space Observatory. *J. Exp. Theor. Phys. Lett.* **108**, 5–12 (2018). 1805.07119.

[21] Choi, G. H. *et al.* Measurement of High-energy Cosmic-Ray Proton Spectrum from the ISS-CREAM Experiment. *Astrophys. J.* **940**, 107 (2022).

[22] Yoon, Y. S. *et al.* Proton and Helium Spectra from the CREAM-III Flight. *Astrophys. J.* **839**, 5 (2017). 1704.02512.

[23] Grebenyuk, V. *et al.* Energy spectra of abundant cosmic-ray nuclei in the NUCLEON experiment. *Adv. Space Res.* **64**, 2546–2558 (2019). 1809.05333.

[24] Kulikov, G. V. & Kristiansen, G. B. On the Size Spectrum of Extensive Air Showers. *Zh. Eksper. Teor. Fiz.* **35**, 635 (1958).

[25] Adriani, O. *et al.* Direct Measurement of the Cosmic-Ray Carbon and Oxygen Spectra from 10 GeV/n to 2.2 TeV/n with the Calorimetric Electron Telescope on the International Space Station. *Phys. Rev. Lett.* **125**, 251102 (2020). 2012.10319.

[26] Aguilar, M. *et al.* Properties of Iron Primary Cosmic Rays: Results from the Alpha Magnetic Spectrometer. *Phys. Rev. Lett.* **126**, 041104 (2021).

[27] Adriani, O. *et al.* Measurement of the Iron Spectrum in Cosmic Rays from 10 GeV/n to 2.0 TeV/n with the Calorimetric Electron Telescope on the International Space Station. *Phys. Rev. Lett.* **126**, 241101 (2021). 2106.08036.

[28] Chang, J. *et al.* The DArk Matter Particle Explorer mission. *Astropart. Phys.* **95**, 6–24 (2017). 1706.08453.

[29] Ambrosi, G. *et al.* Direct detection of a break in the teraelectronvolt cosmic-ray spectrum of electrons and positrons. *Nature* **552**, 63–66 (2017). 1711.10981.

[30] Yu, Y. *et al.* The plastic scintillator detector for DAMPE. *Astropart. Phys.* **94**, 1–10 (2017). 1703.00098.

[31] Azzarello, P. *et al.* The DAMPE silicon–tungsten tracker. *Nucl. Instrum. Meth. A* **831**, 378–384 (2016).

[32] Zhang, Z. *et al.* The calibration and electron energy reconstruction of the BGO ECAL of the DAMPE detector. *Nucl. Instrum. Meth. A* **836**, 98–104 (2016). 1602.07015.

[33] Huang, Y.-Y. *et al.* Calibration and performance of the neutron detector onboard of the

DAMPE mission. *Res. Astron. Astrophys.* **20**, 153 (2020). 2005.07828.

[34] Alemanno, F. *et al.* Observations of Forbush Decreases of Cosmic-Ray Electrons and Positrons with the Dark Matter Particle Explorer. *Astrophys. J. Lett.* **920**, L43 (2021). 2110.00123.

[35] D'Agostini, G. A Multidimensional unfolding method based on Bayes' theorem. *Nucl. Instrum. Meth. A* **362**, 487–498 (1995).

[36] Niu, J.-S. & Liu, J. Quantitative study of the hardening in the Alpha Magnetic Spectrometer nuclei spectra at a few hundred GV. *Front. Astron. Space Sci.* **9**, 1044225 (2022). 2210.08905.

[37] Aguilar, M. *et al.* Observation of New Properties of Secondary Cosmic Rays Lithium, Beryllium, and Boron by the Alpha Magnetic Spectrometer on the International Space Station. *Phys. Rev. Lett.* **120**, 021101 (2018).

[38] Blasi, P., Amato, E. & Serpico, P. D. Spectral breaks as a signature of cosmic ray induced turbulence in the Galaxy. *Phys. Rev. Lett.* **109**, 061101 (2012). 1207.3706.

[39] Lagage, P. O. & Cesarsky, C. J. The maximum energy of cosmic rays accelerated by supernova shocks. *Astron. Astrophys.* **125**, 249–257 (1983).

[40] Zhao, B. *et al.* Geminga SNR: Possible Candidate of the Local Cosmic-Ray Factory. *Astrophys. J.* **926**, 41 (2022). 2104.07321.

[41] Bowman, D. P., Scrandis, R. & Seo, E.-S. Investigating cosmic ray elemental spectra and the atmospheric muon neutrino flux. *Adv. Space Res.* **70**, 2703–2713 (2022).

[42] Recchia, S. & Gabici, S. Origin of the spectral features observed in the cosmic-ray spectrum. *Astron. Astrophys.* **692**, A20 (2024). 2312.11397.

[43] Malkov, M. A. & Moskalenko, I. V. On the Origin of Observed Cosmic-Ray Spectrum Below 100 TV. *Astrophys. J.* **933**, 78 (2022). 2105.04630.

[44] Mertsch, P. & Funk, S. Solution to the cosmic ray anisotropy problem. *Phys. Rev. Lett.* **114**, 021101 (2015). 1408.3630.

[45] Aguilar, M. *et al.* Properties of Cosmic Deuterons Measured by the Alpha Magnetic Spectrometer. *Phys. Rev. Lett.* **132**, 261001 (2024).

DAMPE collaboration

Francesca Alemanno[1,2], Qi An[3,4*], Philipp Azzarello[5], Felicia-Carla-Tiziana Barbato[6,7], Paolo Bernardini[1,2], Xiao-Jun Bi[8,9], Hugo Boutin[5], Irene Cagnoli[6,7], Ming-Sheng Cai[10,11], Elisabetta Casilli[6,7], Jin Chang[10,11], Deng-Yi Chen[10], Jun-Ling Chen[12], Zhan-Fang Chen[12], Zi-Xuan Chen[12,8], Paul Coppin[5], Ming-Yang Cui[10], Tian-Shu Cui[13], Ivan De Mitri[6,7], Francesco de Palma[1,2], Adriano Di Giovanni[6,7], Tie-Kuang Dong[10], Zhen-Xing Dong[13], Giacinto Donvito[14], Jing-Lai Duan[12], Kai-Kai Duan[10], Rui-Rui Fan[9], Yi-Zhong Fan[10,11], Fang Fang[12], Kun Fang[9], Chang-Qing Feng[3,4], Lei Feng[10], Sara Fogliacco[6,7], Jennifer-Maria Frieden[5†], Piergiorgio Fusco[14,15], Min Gao[9], Fabio Gargano[14], Essna Ghose[1,2], Ke Gong[9], Yi-Zhong Gong[10], Dong-Ya Guo[9], Jian-Hua Guo[10,11], Shuang-Xue Han[13], Yi-Ming Hu[10], Guang-Shun Huang[3,4], Xiao-Yuan Huang[10,11], Yong-Yi Huang[10], Maria Ionica[16], Lu-Yao Jiang[10], Wei Jiang[10], Yao-Zu Jiang[16‡], Jie Kong[12], Andrii Kotenko[5], Dimitrios Kyratzis[6,7], Shi-Jun Lei[10], Bo Li[10,11], Manbing Li[5], Wen-Hao Li[10], Wei-Liang Li[13], Xiang Li[10,11], Xian-Qiang Li[13], Yao-Ming Liang[13], Cheng-Ming Liu[16], Hao Liu[10], Jie Liu[12], Shu-Bin Liu[3,4], Yang Liu[10], Francesco Loparco[14,15], Miao Ma[13], Peng-Xiong Ma[10], Tao Ma[10], Xiao-Yong Ma[13], Giovanni Marsella[1,2§], Mario-Nicola Mazziotta[14], Dan Mo[12], Yu Nie[3,4], Xiao-Yang Niu[12], Andrea Parenti[6,7¶], Wen-Xi Peng[9], Xiao-Yan Peng[10], Chiara Perrina[5**], Enzo Putti-Garcia[5], Rui Qiao[9], Jia-Ning Rao[13], Yi Rong[3,4], Ritabrata Sarkar[6,7], Pierpaolo Savina[6,7], Andrea Serpolla[5], Zhi Shangguan[13], Wei-Hua Shen[13], Zhao-Qiang Shen[10], Zhong-Tao Shen[3,4], Leandro Silveri[6,7††], Jing-Xing Song[13], Hong Su[12], Meng Su[17], Hao-Ran Sun[3,4], Zhi-Yu Sun[12], Antonio Surdo[2], Xue-Jian Teng[13], Andrii Tykhonov[5], Gui-Fu Wang[3,4], Jin-Zhou Wang[9], Lian-Guo Wang[13], Shen Wang[10], Xiao-Lian Wang[3,4],

---

* Deceased.

† Now at Institute of Physics, Ecole Polytechnique Fédérale de Lausanne (EPFL), CH-1015 Lausanne, Switzerland.

‡ Also at Dipartimento di Fisica e Geologia, Università degli Studi di Perugia, I-06123 Perugia, Italy.

§ Now at Dipartimento di Fisica e Chimica "E. Segrè", Università degli Studi di Palermo, via delle Scienze ed. 17, I-90128 Palermo, Italy.

¶ Now at Inter-university Institute for High Energies, Universitè Libre de Bruxelles, B-1050 Brussels, Belgium.

** Now at Institute of Physics, Ecole Polytechnique Fédérale de Lausanne (EPFL), CH-1015 Lausanne, Switzerland.

†† Now at New York University Abu Dhabi, Saadiyat Island, Abu Dhabi 129188, United Arab Emirates.

Yan-Fang Wang[3,4], Da-Ming Wei[10,11], Jia-Ju Wei[10], Yi-Feng Wei[3,4], Di Wu[9], Jian Wu[10,11], Sha-Sha Wu[13], Xin Wu[5], Zi-Qing Xia[10], Zheng Xiong[6,7], En-Heng Xu[3,4], Hai-Tao Xu[13], Jing Xu[10], Zhi-Hui Xu[12], Zun-Lei Xu[10], Zi-Zong Xu[3,4], Guo-Feng Xue[13], Ming-Yu Yan[3,4], Hai-Bo Yang[12], Peng Yang[12], Ya-Qing Yang[12], Hui-Jun Yao[12], Yu-Hong Yu[12], Qiang Yuan[10,11], Chuan Yue[10], Jing-Jing Zang[10‡‡], Sheng-Xia Zhang[12], Wen-Zhang Zhang[13], Yan Zhang[10], Ya-Peng Zhang[12], Yi Zhang[10,11], Yong-Jie Zhang[12], Yong-Qiang Zhang[10], Yun-Long Zhang[3,4], Zhe Zhang[10], Zhi-Yong Zhang[3,4], Cong Zhao[3,4], Hong-Yun Zhao[12], Xun-Feng Zhao[13], Chang-Yi Zhou[13], Xun Zhu[10§§], and Yan Zhu[13]

[1] *Dipartimento di Matematica e Fisica E. De Giorgi, Università del Salento, I-73100, Lecce, Italy*

[2] *Istituto Nazionale di Fisica Nucleare (INFN) - Sezione di Lecce, I-73100, Lecce, Italy*

[3] *State Key Laboratory of Particle Detection and Electronics, University of Science and Technology of China, Hefei 230026, China*

[4] *Department of Modern Physics, University of Science and Technology of China, Hefei 230026, China*

[5] *Department of Nuclear and Particle Physics, University of Geneva, CH-1211, Switzerland*

[6] *Gran Sasso Science Institute (GSSI), Via Iacobucci 2, I-67100 L'Aquila, Italy*

[7] *Istituto Nazionale di Fisica Nucleare (INFN) - Laboratori Nazionali del Gran Sasso, I-67100 Assergi, L'Aquila, Italy*

[8] *University of Chinese Academy of Sciences, Beijing 100049, China*

[9] *Particle Astrophysics Division, Institute of High Energy Physics, Chinese Academy of Sciences, Beijing 100049, China*

[10] *Key Laboratory of Dark Matter and Space Astronomy, Purple Mountain Observatory, Chinese Academy of Sciences, Nanjing 210023, China*

[11] *School of Astronomy and Space Science, University of Science and Technology of China, Hefei 230026, China*

[12] *State Key Laboratory of Heavy Ion Science and Technology, Institute of Modern Physics, Chinese Academy of Sciences, Lanzhou 730000, China*

[13] *National Space Science Center, Chinese Academy of Sciences, Nanertiao 1, Zhongguancun, Haidian district, Beijing 100190, China*

‡‡ Also at School of Physics and Electronic Engineering, Linyi University, Linyi 276000, China.
§§ Also at School of computing, Nanjing University of Posts and Telecommunications, Nanjing 210023, China.

[14] *Istituto Nazionale di Fisica Nucleare, Sezione di Bari, via Orabona 4, I-70126 Bari, Italy*

[15] *Dipartimento di Fisica "M. Merlin", dell'Università e del Politecnico di Bari, via Amendola 173, I-70126 Bari, Italy*

[16] *Istituto Nazionale di Fisica Nucleare (INFN) - Sezione di Perugia, I-06123 Perugia, Italy*

[17] *Department of Physics and Laboratory for Space Research, the University of Hong Kong, Hong Kong SAR, China*

Supplemental Materials

DAMPE experiment

The DAMPE satellite was launched into a 500-km Sun-synchronous orbit on December 17, 2015, and has operated stably in space since then. The on-orbit calibration of each detector shows that the payload has maintained a good long-term performance over the past years[46]. Also, the detector performance was validated with test beams of protons, electrons and fragmented ions with $A/Z = 2$ from helium to argon. The linearity of the energy measurement of DAMPE is validated with the electron beams up to 243 GeV[32]. At higher energies, the laser test suggested that the measurement of the deposited energy in a single BGO crystal retains a good linearity up to a few TeV[47]. The absolute energy scale of DAMPE is determined with the geomagnetic cutoff of the electron plus positron spectrum, which results in a small bias of $\sim$1.3%[48] and is not corrected.

Monte Carlo simulation

Extensive MC simulations are carried out to obtain the instrument response to incident particles in the DAMPE detector. The GEometry ANd Tracking (GEANT) toolkit v4.10.05[49] with the FTFP_BERT physics list is adopted for the simulations of nuclei up to 100 TeV/n. For higher energies, we use the EPOS_LHC model from the the Cosmic Ray Monte Carlo (CRMC; https://web.ikp.kit.edu/rulrich/crmc.html) linked to GEANT through a custom interface[50]. The energy response of MC simulations is corrected by including the Birks' quenching effect when calculating the ionization energy deposits in the calorimeter[51]. Such a correction is important for high Z and low energy particles.

The simulated events are generated assuming an isotropic source with an E^{-1} spectrum. The simulation data are re-weighted to $E^{-2.6}$ and $E^{-3.0}$ spectra, for primary (e.g. carbon, oxygen, and iron) and secondary (e.g. boron) nuclei, respectively. To evaluate the uncertainties from the hadronic interaction model, another simulation program is developed with the FLUKA[52] 2011.2x package, which uses DPMJET3 for nucleus-nucleus interaction above 5 GeV/n.

Event selections

Given that the analysis procedures for protons and helium nuclei closely follow those established in refs.[14] and [15], the present work focuses primarily on the analysis of carbon, oxygen, and iron nuclei. Nine years of on-orbit data are used with a total exposure time of

$\sim 2.17 \times 10^8$ s, corresponding to ∼76.2% of the operation time. A general pre-selection is applied to select events with good quality of reconstruction. The selection logic for different nuclei is broadly consistent, although the specific parameters are adjusted accordingly.

(I) **Pre-selection.** The pre-selection is to ensure good shower development and proper event reconstruction in the calorimeter, including:

(i) the total deposited energy ($E_{\rm dep}$) must exceed 50 GeV, 63 GeV, and 150 GeV for carbon, oxygen, and iron nuclei, respectively, to minimize the geomagnetic cutoff effect[53];

(ii) the energy deposited in any single BGO layer must not exceed 35% of the total deposited energy to exclude events incident from the sides.

(II) **Trigger condition.** Events satisfying the High Energy Trigger (HET) condition[28] are selected. The HET is optimized to select well-contained events. For carbon, oxygen, and iron nuclei, the HET efficiency exceeds 95%.

(III) **Track selection.** A deep learning based tracking approach[54] is employed, which achieves a better performance especially at high energies than the Kalman filter track reconstruction. The reconstructed track is further required to align with the maximum number of hits in both the PSD-x and PSD-y layers and to penetrate the calorimeter from top to bottom. This ensures that the event is fully contained within the detector and the key characteristics can be accurately measured.

(IV) **Charge selection.** The particle charge Z is measured by both the PSD and the STK. For carbon and oxygen, the first STK layer charge is required to satisfy $Q_{\rm STK1} > 2.8$ to suppress contamination from protons and helium nuclei. For PSD charge measurement, the signals from the four sub-layers are employed to build a global PSD charge, with proper corrections due to strip alignments, light attenuation, fluorescence quenching, and equalization of different channels[55, 56]. The candidate events are selected using energy-dependent charge intervals as:

$$\begin{aligned} 5.7 < Q_{\rm PSD} < 6.3 + 0.015 \cdot \log^2(E_{\rm dep}/{\rm GeV}), \quad \text{(for carbon)}, \\ 7.7 < Q_{\rm PSD} < 8.35 + 0.015 \cdot \log^2(E_{\rm dep}/{\rm GeV}), \quad \text{(for oxygen)}, \\ 25.5 < Q_{\rm PSD} < 27.2 \quad \text{(for iron)}. \end{aligned}$$

The charge selection criteria maintain an efficiency of approximately 90% over the full analysis energy range. The same procedure and selections are applied to the MC simulations, and the MC charge distributions are shrinked to match the flight data for different particles. For proton and helium analysis, a combination of the PSD and STK charge measurements is employed to keep a stable selection efficiency at high energies (> 10 TeV).

Background subtraction

An MC-based template fit is performed on the charge distribution to estimate the background contamination within the selected charge windows for each species, as shown in as shown in Figure S1. In these figures, the hatched regions show the GEANT4 simulated charge distributions of given particle species, and the red solid lines show the total contribution of relevant species. Good match between the data and the simulation can be obtained.

The contamination for target nuclei are estimated through computing the fractions of adjacent nuclei in the specified charge window according to the MC templates. For proton and helium, their cross-contamination dominate the backgrounds, which are estimated to be less than 4% and 5%, respectively, in the whole energy range. For carbon, in the lower-energy region, the dominant background arises from the fragmentation of heavier nuclei (particularly oxygen). At high energies, above the TeV scale, high-abundance helium nuclei can produce showers in the calorimeter that spawn back-scattered secondaries penetrating the PSD strips. This leads to an overestimation of the reconstructed charge and introduces a non-negligible contamination in both carbon and oxygen samples. Consequently, the total contamination ratios for carbon and oxygen increase from 0.5% and 0.4% at 100 GeV to 2.4% and 1.8% at 50 TeV, respectively. For iron, both lighter nuclei (chromium, manganese) and heavier ones (e.g., cobalt and nickel) are far less abundant than iron itself. Moreover, the iron signal is sufficiently large that the impact of back-scattered shower particles on charge reconstruction is negligible. Therefore, the contamination ratio of the iron sample remains within 3% in the whole energy range.

CR flux measurements

The total deposited energy in the calorimeter (E_{dep}) is measured by summing up the energies of all BGO bars together. When the energy deposited in a single BGO bar exceeds ~ 4 TeV, some readout channels may saturate[57], leading to non-linearity in the energy response. A

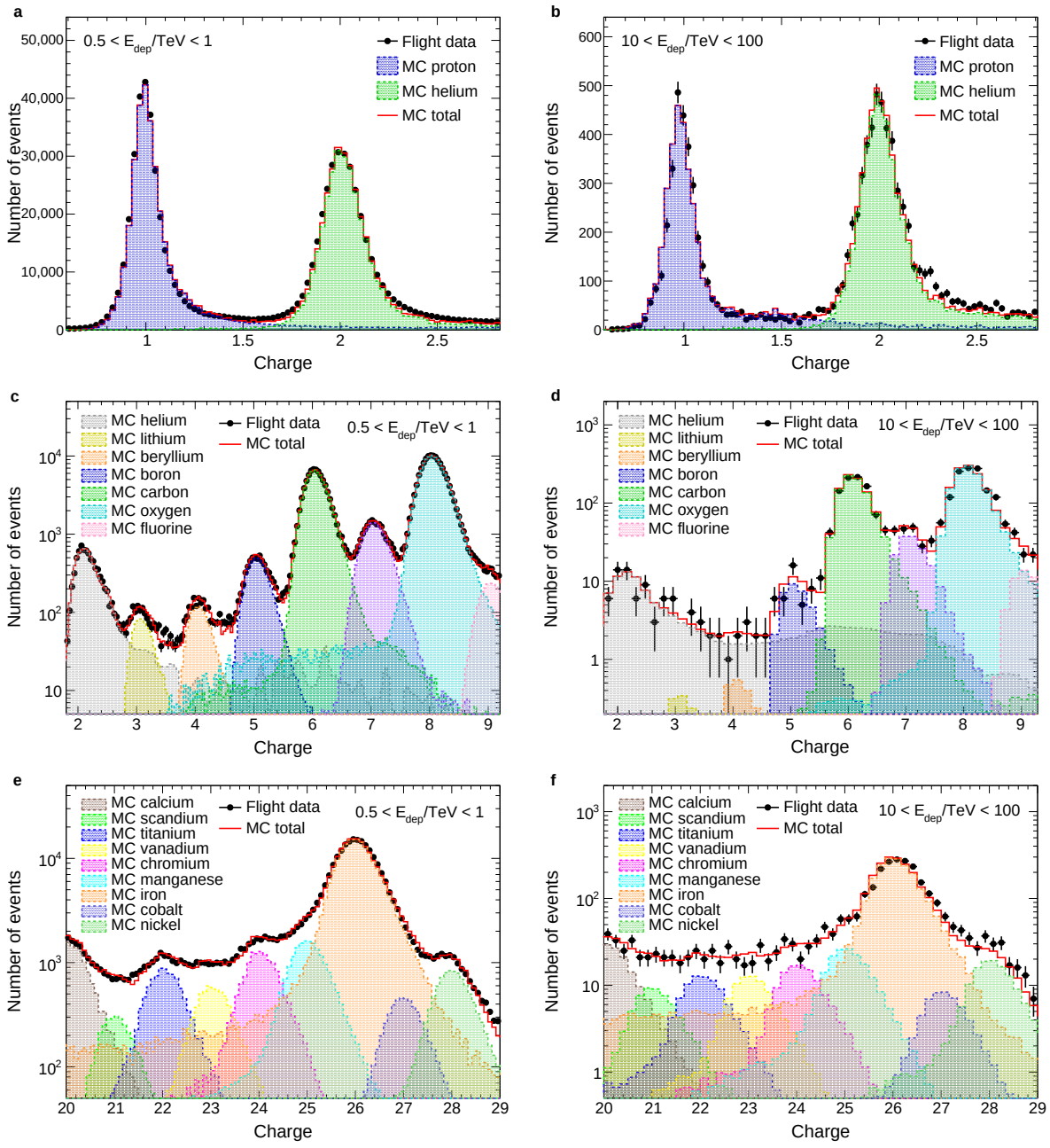

FIG. S1: **Charge distributions of events.** The left panels (**a**, **c**, **e**) are for deposited energy bin of $0.5 < E_{\rm dep} < 1$ TeV, and the right panels (**b**, **d**, **f**) are for deposited energy bin of $10 < E_{\rm dep} < 100$ TeV. From top to bottom, three charge ranges relevant to protons and helium, carbon and oxygen, and iron nuclei are shown. Black dots depict the flight data. Dashed lines with different colors show the best-fit MC simulated samples. The red solid lines show the sum of MC samples.

deep learning approach[58] based on MC simulation was developed to correct the energy

deposit(s) of those saturated bar(s) for nuclei up to PeV. Due to the relatively large spread of the calorimeter's energy response to the nuclei, an unfolding procedure[35] is employed to derive the primary fluxes of CRs. The differential flux in a given incident energy bin $[E_i, E_i + \Delta E_i]$ is then calculated as

$$\Phi(E_i, E_i + \Delta E_i) = \frac{N_{\mathrm{inc},i}}{\Delta E_i \ A_{\mathrm{eff},i} \ \Delta t}, \tag{1}$$

where ΔE_i is the energy bin width, $A_{\mathrm{eff},i}$ is the effective acceptance, and Δt is the live time. The unfolded number of events, $N_{\mathrm{inc},i}$, is given by

$$N_{\mathrm{inc},i} = \sum_{j=1}^{n} P(E_i|W_j) N_{\mathrm{dep},j}, \tag{2}$$

where $N_{\mathrm{dep},j}$ is the number of events in the j-th deposit energy bin $[W_j, W_j + \Delta W_j]$, and $P(E_i|W_j)$ is the transfer probability from the j-th deposit energy bin to the i-th incident energy bin.

The effective acceptance in the i-th kinetic energy bin is estimated from MC samples as

$$A_{\mathrm{eff},i} = G_{\mathrm{gen}} \times \frac{N_i^{\mathrm{sel}}}{N_i^{\mathrm{gen}}}, \tag{3}$$

where G_{gen} is the geometric factor corresponding to the generation surface in the MC simulation, N_i^{gen} is the number of generated events in the i-th energy bin, and N_i^{sel} is the number of events that pass all of the selection criteria.

Uncertainties

The statistical uncertainties are associated with Poisson fluctuations of the number of detected events $N(E_{\mathrm{dep,j}})$. To properly determine the error propagation in the unfolding procedure, a toy-MC approach is applied, via sampling the event numbers in each deposited energy bin with Poisson fluctuations. The variations of the unfolded numbers of events in each kinetic energy bin are then obtained and the standard deviations are assigned as the 1σ statistical uncertainty.

The systematic uncertainties due to different sources are investigated extensively. The selection efficiencies derived from the MC simulation, e.g. HET and track, are compared with the efficiencies estimated from the flight data for different particles and the deviations are taken as the associated systematic uncertainties. The uncertainty of charge selection is estimated by varying the charge selection window and checking the flux variations. The uncertainty due to background subtraction is estimated by considering the errors of the

contamination fractions from the template fit procedure. The uncertainty from the BGO saturation correction is obtained by artificially modifying the energy correction for the saturated events by ±1 standard deviation of the corrected ratio variation.

For proton and helium, the related uncertainties are found to be significantly below 1% up to 200 TeV and thus negligible in the current flux measurements. Finally, the systematic uncertainty associated with the hadronic interaction model used in the MC simulation is obtained through comparing simulation results with the test beam data or two different simulation tools, i.e. GEANT4 and FLUKA. Specifically, for proton, helium, carbon and oxygen, the uncertainty of the hadronic interaction model in lower energy region ($<$ 400 GeV for proton and $<$ 75 GeV/n for others) is estimated according to the comparison of the energy response between the test beam data and the GEANT4 simulation. At higher energies, the uncertainty is assigned as the difference between the fluxes measured using the GEANT4 and the FLUKA simulations. For iron, no beam test data is available and hence the uncertainty is evaluated as the difference between the two simulations.

The total uncertainty budgets for proton, helium, carbon, oxygen and iron are shown in Figure S2. The measured fluxes and the associated uncertainties, including the statistical uncertainties and systematic ones from the analysis procedure and the hadronic interaction models, are presented in Tables S1, S2, S3, S4, and S5.

Spectral fitting

The significance of the spectral hardening or softening feature is estimated by comparing the fittings with two different models. One is a power-law (PL) function

$$\Phi_{\rm PL}(E) = \Phi_0 \cdot \left(\frac{E}{10^3\ {\rm GeV}}\right)^{-\gamma}, \tag{4}$$

and the other is a Smoothly Broken Power Law (SBPL) function

$$\Phi_{\rm SBPL}(E) = \Phi_0 \cdot \left(\frac{E}{10^3\ {\rm GeV}}\right)^{-\gamma} \left[1 + \left(\frac{E}{E_{\rm br}}\right)^{s}\right]^{\frac{\Delta\gamma}{s}}, \tag{5}$$

where γ is the spectral index below the break energy $E_{\rm br}$, $\Delta\gamma$ is the change of the spectral index and and s is the smoothness parameter.

The same fit method as refs.[14] and [15] is applied to account for the systematic uncertainties by multiplying a set of independent nuisance parameters w_j on the input model[59].

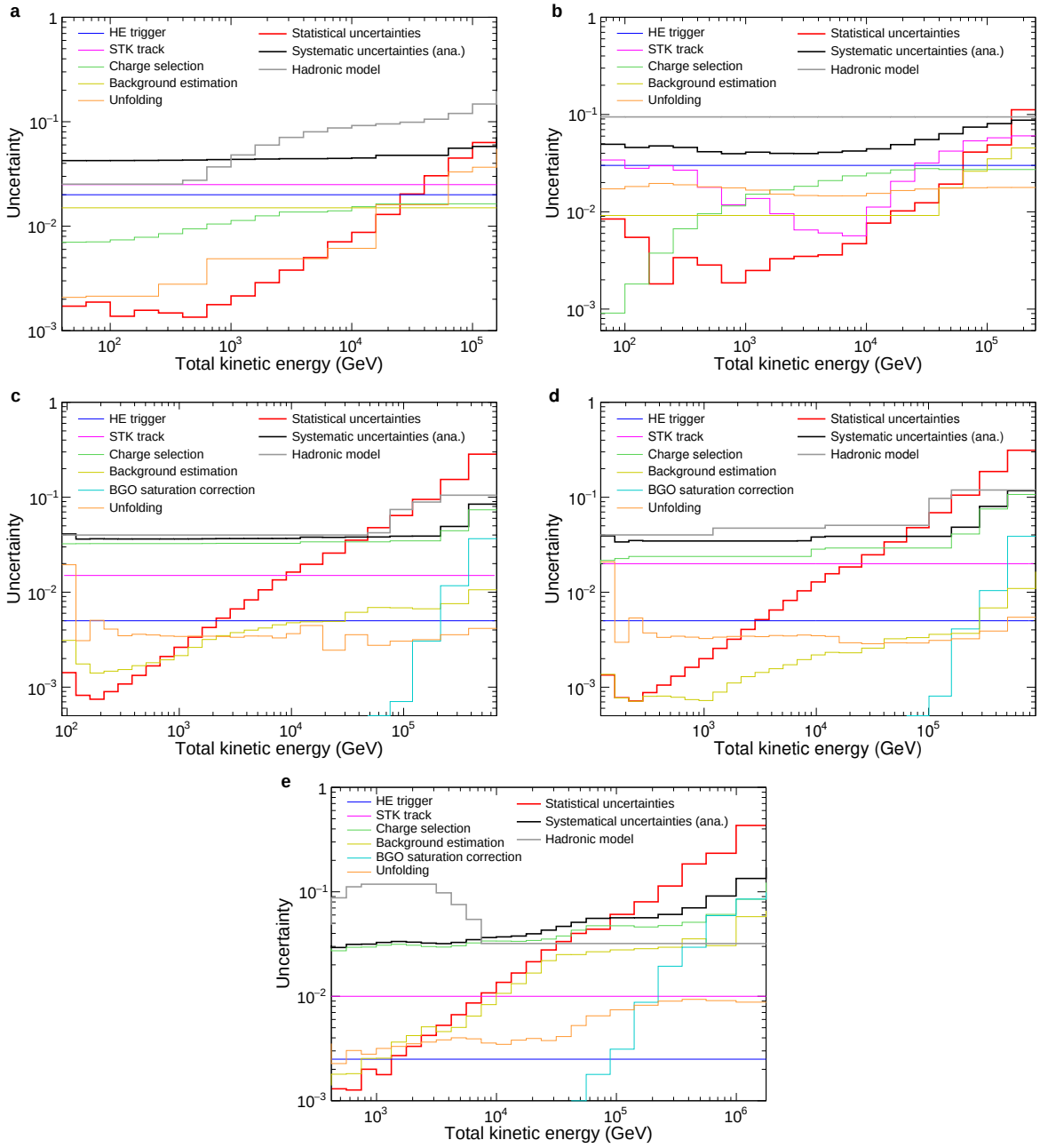

FIG. S2: **Relative uncertainties versus energy.** Panels **a** - **e** correspond to those of proton, helium, carbon, oxygen, and iron, respectively. The systematic uncertainties in analysis, shown in black, are the quadratic sum of all systematic contributions except for those from the hadronic models.

TABLE S1: The proton fluxes as function of total kinetic energy (E_t) measured by DAMPE, together with the 1σ statistical errors and the systematic uncertainties from the analysis and hadronic interaction models.

E_t Bin (GeV)	$\Phi \pm \sigma_{\rm stat} \pm \sigma_{\rm sys}^{\rm ana} \pm \sigma_{\rm sys}^{\rm had}$ (GeV^{-1} m^{-2} s^{-1} sr^{-1})
39.8 - 63.1	$(2.81 \pm 0.005 \pm 0.12 \pm 0.07) \times 10^{-1}$
63.1 - 100.0	$(8.05 \pm 0.015 \pm 0.34 \pm 0.20) \times 10^{-2}$
100.0 - 158.5	$(2.27 \pm 0.003 \pm 0.10 \pm 0.06) \times 10^{-2}$
158.5 - 251.2	$(6.36 \pm 0.010 \pm 0.27 \pm 0.16) \times 10^{-3}$
251.2 - 398.1	$(1.81 \pm 0.003 \pm 0.08 \pm 0.05) \times 10^{-3}$
398.1 - 631.0	$(5.23 \pm 0.007 \pm 0.22 \pm 0.14) \times 10^{-4}$
631.0 - 1000	$(1.54 \pm 0.003 \pm 0.07 \pm 0.06) \times 10^{-4}$
1000 - 1585	$(4.60 \pm 0.010 \pm 0.20 \pm 0.22) \times 10^{-5}$
1585 - 2512	$(1.39 \pm 0.004 \pm 0.06 \pm 0.08) \times 10^{-5}$
2512 - 3981	$(4.24 \pm 0.015 \pm 0.19 \pm 0.30) \times 10^{-6}$
3981 - 6310	$(1.30 \pm 0.006 \pm 0.06 \pm 0.11) \times 10^{-6}$
6310 - 10000	$(3.99 \pm 0.027 \pm 0.18 \pm 0.35) \times 10^{-7}$
10000 - 15849	$(1.18 \pm 0.010 \pm 0.05 \pm 0.11) \times 10^{-7}$
15849 - 25119	$(3.34 \pm 0.043 \pm 0.16 \pm 0.32) \times 10^{-8}$
25119 - 39811	$(8.85 \pm 0.190 \pm 0.42 \pm 0.88) \times 10^{-9}$
39811 - 63096	$(2.30 \pm 0.073 \pm 0.11 \pm 0.25) \times 10^{-9}$
63096 - 100000	$(6.05 \pm 0.281 \pm 0.34 \pm 0.73) \times 10^{-10}$
100000 - 158489	$(1.69 \pm 0.109 \pm 0.10 \pm 0.25) \times 10^{-10}$

The χ^2 function is defined as

$$\chi^2 = \sum_i \left[\frac{\Phi(E_i) S(E_i;\, \boldsymbol{w}) - \Phi_i}{\sigma_{\rm stat,i}} \right]^2 + \sum_{j=1}^{m} \left(\frac{1 - w_j}{\tilde{\sigma}_{\rm sys,j}} \right)^2 , \tag{6}$$

where Φ_i and $\sigma_{\rm stat,i}$ are the flux and statistical uncertainty of the measurement in the ith kinetic energy bin, $\Phi(E_i)$ is the predicted flux in corresponding energy bin, $S(E_i;\, \boldsymbol{w})$ is a piecewise function defined by its value w_j in corresponding energy range covered by the jth nuisance parameter, and $\tilde{\sigma}_{\rm sys,j} = \sqrt{\sigma_{\rm ana}^2 + \sigma_{\rm had}^2}/\Phi$ is the relative systematic uncertainty of

TABLE S2: The helium fluxes as function of total kinetic energy (E_t) measured by DAMPE, together with the 1σ statistical errors and the systematic uncertainties from the analysis and hadronic interaction models.

E_t Bin (GeV)	$\Phi \pm \sigma_{\rm stat} \pm \sigma_{\rm sys}^{\rm ana} \pm \sigma_{\rm sys}^{\rm had}$ (GeV^{-1} m^{-2} s^{-1} sr^{-1})
63.1 - 100.0	$(5.31 \pm 0.045 \pm 0.28 \pm 0.50) \times 10^{-2}$
100.0 - 158.5	$(1.60 \pm 0.009 \pm 0.08 \pm 0.15) \times 10^{-2}$
158.5 - 251.2	$(4.56 \pm 0.083 \pm 0.24 \pm 0.43) \times 10^{-3}$
251.2 - 398.1	$(1.30 \pm 0.004 \pm 0.07 \pm 0.12) \times 10^{-3}$
398.1 - 631.0	$(3.81 \pm 0.011 \pm 0.18 \pm 0.36) \times 10^{-4}$
631.0 - 1000	$(1.13 \pm 0.002 \pm 0.05 \pm 0.11) \times 10^{-4}$
1000 - 1585	$(3.42 \pm 0.009 \pm 0.16 \pm 0.32) \times 10^{-5}$
1585 - 2512	$(1.05 \pm 0.003 \pm 0.05 \pm 0.10) \times 10^{-5}$
2512 - 3981	$(3.31 \pm 0.012 \pm 0.15 \pm 0.31) \times 10^{-6}$
3981 - 6310	$(1.06 \pm 0.004 \pm 0.05 \pm 0.10) \times 10^{-6}$
6310 - 10000	$(3.47 \pm 0.016 \pm 0.16 \pm 0.33) \times 10^{-7}$
10000 - 15849	$(1.16 \pm 0.009 \pm 0.06 \pm 0.11) \times 10^{-7}$
15849 - 25119	$(3.82 \pm 0.039 \pm 0.20 \pm 0.36) \times 10^{-8}$
25119 - 39811	$(1.21 \pm 0.015 \pm 0.07 \pm 0.11) \times 10^{-8}$
39811 - 63096	$(3.57 \pm 0.069 \pm 0.24 \pm 0.34) \times 10^{-9}$
63096 - 100000	$(1.01 \pm 0.042 \pm 0.08 \pm 0.10) \times 10^{-9}$
100000 - 158489	$(2.85 \pm 0.139 \pm 0.24 \pm 0.27) \times 10^{-10}$
158489 - 251189	$(8.52 \pm 0.954 \pm 0.78 \pm 0.81) \times 10^{-11}$

the data in such an energy range. When calculating $\Phi(E_i)$, the flux at the central energy of each bin is used, which results in negligible differences of the fitting parameters compared with the method of integrating the fluxes over the energy bin.

The fit parameters of the SBPL model for the hardening and softening features are presented in Tables S6 and S7, respectively. For the fit for the softening features, the smoothness parameter s is fixed as 5 or 10 due to a lack of good constraint on it. The significances of those spectral features are evaluated by the comparisons of the χ^2 values

TABLE S3: The carbon fluxes as function of total kinetic energy (E_t) measured by DAMPE, together with the 1σ statistical errors and the systematic uncertainties from the analysis and hadronic interaction models.

E_t Bin (GeV)	$\Phi \pm \sigma_{\rm stat} \pm \sigma_{\rm sys}^{\rm ana} \pm \sigma_{\rm sys}^{\rm had}$ (GeV^{-1} m^{-2} s^{-1} sr^{-1})
90.0 - 120.0	$(4.60 \pm 0.007 \pm 0.19 \pm 0.18) \times 10^{-3}$
120.0 - 160.0	$(2.29 \pm 0.002 \pm 0.08 \pm 0.09) \times 10^{-3}$
160.0 - 213.4	$(1.11 \pm 0.001 \pm 0.04 \pm 0.04) \times 10^{-3}$
213.4 - 284.6	$(5.26 \pm 0.005 \pm 0.19 \pm 0.21) \times 10^{-4}$
284.6 - 379.5	$(2.48 \pm 0.003 \pm 0.09 \pm 0.10) \times 10^{-4}$
379.5 - 506.0	$(1.17 \pm 0.002 \pm 0.04 \pm 0.05) \times 10^{-4}$
506.0 - 674.8	$(5.44 \pm 0.009 \pm 0.20 \pm 0.22) \times 10^{-5}$
674.8 - 899.9	$(2.51 \pm 0.005 \pm 0.09 \pm 0.10) \times 10^{-5}$
899.9 - 1200	$(1.17 \pm 0.003 \pm 0.04 \pm 0.05) \times 10^{-5}$
1200 - 1600	$(5.43 \pm 0.018 \pm 0.20 \pm 0.22) \times 10^{-6}$
1600 - 2134	$(2.53 \pm 0.011 \pm 0.09 \pm 0.10) \times 10^{-6}$
2134 - 2846	$(1.18 \pm 0.006 \pm 0.04 \pm 0.05) \times 10^{-6}$
2846 - 3795	$(5.54 \pm 0.037 \pm 0.20 \pm 0.22) \times 10^{-7}$
3795 - 5060	$(2.64 \pm 0.022 \pm 0.10 \pm 0.11) \times 10^{-7}$
5060 - 6748	$(1.27 \pm 0.014 \pm 0.05 \pm 0.05) \times 10^{-7}$
6748 - 8999	$(6.07 \pm 0.082 \pm 0.22 \pm 0.24) \times 10^{-8}$
8999 - 12000	$(2.96 \pm 0.049 \pm 0.11 \pm 0.12) \times 10^{-8}$
12000 - 19019	$(1.20 \pm 0.024 \pm 0.05 \pm 0.05) \times 10^{-8}$
19019 - 30143	$(3.86 \pm 0.101 \pm 0.15 \pm 0.16) \times 10^{-9}$
30143 - 47773	$(1.29 \pm 0.046 \pm 0.05 \pm 0.05) \times 10^{-9}$
47773 - 75715	$(4.62 \pm 0.022 \pm 0.18 \pm 0.20) \times 10^{-10}$
75715 - 120000	$(1.52 \pm 0.098 \pm 0.06 \pm 0.11) \times 10^{-10}$
120000 - 213394	$(3.69 \pm 0.350 \pm 0.14 \pm 0.33) \times 10^{-11}$
213394 - 379474	$(7.37 \pm 1.135 \pm 0.36 \pm 0.78) \times 10^{-12}$
379474 - 674809	$(1.48 \pm 0.421 \pm 0.12 \pm 0.16) \times 10^{-12}$

TABLE S4: The oxygen fluxes as function of total kinetic energy (E_t) measured by DAMPE, together with the 1σ statistical errors and the systematic uncertainties from the analysis and hadronic interaction models.

E_t Bin (GeV)	$\Phi \pm \sigma_{\rm stat} \pm \sigma_{\rm sys}^{\rm ana} \pm \sigma_{\rm sys}^{\rm had}$ ($\rm GeV^{-1}\ m^{-2}\ s^{-1}\ sr^{-1}$)
120.0 - 160.0	$(3.47 \pm 0.005 \pm 0.14 \pm 0.14) \times 10^{-3}$
160.0 - 213.4	$(1.77 \pm 0.001 \pm 0.06 \pm 0.07) \times 10^{-3}$
213.4 - 284.5	$(8.66 \pm 0.006 \pm 0.30 \pm 0.35) \times 10^{-4}$
284.5 - 379.4	$(4.19 \pm 0.004 \pm 0.15 \pm 0.17) \times 10^{-4}$
379.4 - 506.0	$(2.01 \pm 0.002 \pm 0.07 \pm 0.08) \times 10^{-4}$
506.0 - 674.7	$(9.47 \pm 0.012 \pm 0.33 \pm 0.38) \times 10^{-5}$
674.7 - 899.7	$(4.46 \pm 0.007 \pm 0.15 \pm 0.18) \times 10^{-5}$
899.7 - 1200	$(2.08 \pm 0.004 \pm 0.07 \pm 0.08) \times 10^{-5}$
1200 - 1600	$(9.66 \pm 0.025 \pm 0.33 \pm 0.46) \times 10^{-6}$
1600 - 2134	$(4.50 \pm 0.014 \pm 0.16 \pm 0.21) \times 10^{-6}$
2134 - 2845	$(2.09 \pm 0.008 \pm 0.07 \pm 0.10) \times 10^{-6}$
2845 - 3794	$(9.69 \pm 0.050 \pm 0.34 \pm 0.46) \times 10^{-7}$
3794 - 5060	$(4.51 \pm 0.029 \pm 0.16 \pm 0.21) \times 10^{-7}$
5060 - 6747	$(2.13 \pm 0.017 \pm 0.07 \pm 0.10) \times 10^{-7}$
6747 - 8997	$(1.03 \pm 0.010 \pm 0.04 \pm 0.05) \times 10^{-7}$
8997 - 11998	$(5.00 \pm 0.064 \pm 0.19 \pm 0.24) \times 10^{-8}$
11998 - 16000	$(2.46 \pm 0.038 \pm 0.09 \pm 0.12) \times 10^{-8}$
16000 - 25358	$(9.88 \pm 0.182 \pm 0.38 \pm 0.50) \times 10^{-9}$
25358 - 40190	$(3.21 \pm 0.080 \pm 0.12 \pm 0.16) \times 10^{-9}$
40190 - 63697	$(1.04 \pm 0.035 \pm 0.04 \pm 0.05) \times 10^{-9}$
63697 - 100953	$(3.37 \pm 0.162 \pm 0.13 \pm 0.17) \times 10^{-10}$
100953 - 160000	$(1.04 \pm 0.071 \pm 0.04 \pm 0.10) \times 10^{-10}$
160000 - 284525	$(2.39 \pm 0.252 \pm 0.12 \pm 0.28) \times 10^{-11}$
284525 - 505965	$(4.34 \pm 0.810 \pm 0.35 \pm 0.52) \times 10^{-12}$
505965 - 899746	$(7.88 \pm 0.248 \pm 0.92 \pm 0.94) \times 10^{-13}$

TABLE S5: The iron fluxes as function of total kinetic energy (E_t) measured by DAMPE, together with the 1σ statistical errors and the systematic uncertainties from the analysis and hadronic interaction models.

E_t Bin (GeV)	$\Phi \pm \sigma_{\rm stat} \pm \sigma_{\rm sys}^{\rm ana} \pm \sigma_{\rm sys}^{\rm had}$ (GeV^{-1} m^{-2} s^{-1} sr^{-1})
419.9 - 560.0	$(1.21 \pm 0.002 \pm 0.04 \pm 0.11) \times 10^{-4}$
560.0 - 746.8	$(6.32 \pm 0.008 \pm 0.20 \pm 0.71) \times 10^{-5}$
746.8 - 995.8	$(3.21 \pm 0.006 \pm 0.10 \pm 0.38) \times 10^{-5}$
995.8 - 1328	$(1.62 \pm 0.003 \pm 0.05 \pm 0.19) \times 10^{-5}$
1328 - 1771	$(7.99 \pm 0.022 \pm 0.27 \pm 0.95) \times 10^{-6}$
1771 - 2362	$(3.89 \pm 0.013 \pm 0.13 \pm 0.46) \times 10^{-6}$
2362 - 3149	$(1.89 \pm 0.008 \pm 0.06 \pm 0.22) \times 10^{-6}$
3149 - 4199	$(9.01 \pm 0.047 \pm 0.30 \pm 0.88) \times 10^{-7}$
4199 - 5600	$(4.20 \pm 0.028 \pm 0.13 \pm 0.32) \times 10^{-7}$
5600 - 7468	$(1.95 \pm 0.017 \pm 0.07 \pm 0.11) \times 10^{-7}$
7468 - 9958	$(9.06 \pm 0.098 \pm 0.33 \pm 0.29) \times 10^{-8}$
9958 - 13280	$(4.37 \pm 0.059 \pm 0.16 \pm 0.14) \times 10^{-8}$
13280 - 17709	$(2.12 \pm 0.035 \pm 0.08 \pm 0.07) \times 10^{-8}$
17709 - 23615	$(1.01 \pm 0.022 \pm 0.04 \pm 0.03) \times 10^{-8}$
23615 - 31491	$(4.75 \pm 0.132 \pm 0.21 \pm 0.15) \times 10^{-9}$
31491 - 41994	$(2.33 \pm 0.078 \pm 0.10 \pm 0.07) \times 10^{-9}$
41994 - 56000	$(1.17 \pm 0.047 \pm 0.06 \pm 0.04) \times 10^{-9}$
56000 - 88754	$(4.69 \pm 0.206 \pm 0.27 \pm 0.15) \times 10^{-10}$
88754 - 140666	$(1.47 \pm 0.089 \pm 0.09 \pm 0.05) \times 10^{-10}$
140666 - 222940	$(4.84 \pm 0.388 \pm 0.27 \pm 0.15) \times 10^{-11}$
222940 - 353336	$(1.56 \pm 0.177 \pm 0.10 \pm 0.05) \times 10^{-11}$
353336 - 560000	$(4.30 \pm 0.795 \pm 0.38 \pm 0.14) \times 10^{-12}$
560000 - 995837	$(8.84 \pm 2.068 \pm 0.95 \pm 0.28) \times 10^{-13}$
995837 - 1770876	$(1.32 \pm 0.589 \pm 0.19 \pm 0.04) \times 10^{-13}$

for the PL and SBPL models. For the hardening, the reduction of the χ^2/dof is 867.4/3, 562.2/3, 128.5/3, 110.1/3 and 11.4/2, corresponding to significance of 29σ, 23σ, 11σ, 10σ, and 2.7σ for proton, helium, carbon, oxygen, and iron, respectively. While, for the softening, the reduction of the χ^2/dof is 102.5/2, 58.2/2, 14.7/2, 21.6/2 and 9.6/2, corresponding to significance of 9.1σ, 7.2σ, 3.2σ, 4.1σ, and 2.4σ for proton, helium, carbon, oxygen, and iron, respectively.

TABLE S6: The parameters of the SBPL model obtained from the fit of the spectral hardening features for proton, helium, carbon, oxygen and iron.

Particle	Proton	Helium	Carbon	Oxygen	Iron
Fit energy range	0.063 - 6.3 TeV	0.100 - 15.8 TeV	0.506 - 47.8 TeV	0.675 - 63.7 TeV	1.77 - 223 TeV
Nuisance parameters	4	4	4	4	4
Φ_0 (10^{-5} GeV^{-1} m^{-2} s^{-1} sr^{-1})	7.11 ± 0.26	5.57 ± 0.34	1.28 ± 0.04	2.27 ± 0.07	2.55 ± 0.11
$E_{\rm br}$ (TeV)	0.59 ± 0.04	1.19 ± 0.08	5.35 ± 1.26	6.39 ± 0.61	28.7 ± 11.3
γ	2.77 ± 0.01	2.72 ± 0.01	2.68 ± 0.01	2.66 ± 0.01	2.60 ± 0.01
$\Delta\gamma$	0.21 ± 0.02	0.28 ± 0.03	0.26 ± 0.05	0.21 ± 0.03	0.15 ± 0.05
s	1.70 ± 0.23	2.05 ± 0.42	2.12 ± 0.84	5.86 ± 2.97	5 (fixed)

TABLE S7: The parameters of the SBPL model obtained from the fit of the spectral softening features for proton, helium, carbon, oxygen and iron.

Particle	Proton	Helium	Carbon	Oxygen	Iron
Fit energy range	1.58 - 100 TeV	3.98 - 250 TeV	19.0 - 675 TeV	9.0 - 900 TeV	236 - 1771 TeV
Nuisance parameters	3	3	2	3	3
Φ_0 (10^{-5} GeV^{-1} m^{-2} s^{-1} sr^{-1})	8.08 ± 0.48	5.03 ± 0.35	0.60 ± 0.12	1.54 ± 0.16	1.50 ± 0.47
$E_{\rm br}$ (TeV)	14.6 ± 1.3	30.6 ± 4.4	96.5 ± 33.5	123 ± 38	360 ± 157
γ	2.57 ± 0.01	2.40 ± 0.01	2.32 ± 0.06	2.45 ± 0.03	2.46 ± 0.05
$\Delta\gamma$	-0.34 ± 0.05	-0.32 ± 0.07	-0.49 ± 0.17	-0.48 ± 0.18	-0.69 ± 0.41
s	5 (fixed)	5 (fixed)	10 (fixed)	10 (fixed)	10 (fixed)

Interpretations

(I) The background plus nearby source model. This model assumes that the ensemble of many sources contributes to the majority of the observed CRs (called as background), with the addition of a nearby one which gives distinct features from the background. We adopt the GALPROP propagation code[60] to calculate the fluxes from the background

component. The propagation halo is characterized by a cylinder with radius r_h and half-height z_h. We work in a two-halo propagation framework as indicated by the slow diffusion of particles in the vicinities of middle-aged pulsars[61, 62]. To reproduce the observed breaks of the secondary-to-primary ratios[16], the rigidity-dependence of the diffusion coefficient in the Milky Way halo is parameters as a broken PL form, $D_{\rm halo}(R) = \beta D_0 (R/{\rm GV})^{\delta_1}[1 + (R/R_{\rm br})^2]^{(\delta_2-\delta_1)/2}$, where δ_1 and δ_2 are the slopes below and above $R_{\rm br}$, β is the particle velocity in unit of light speed. The diffusion coefficients in the disk and halo connect with each other smoothly, via $D_{\rm disk} = f(z) D_{\rm halo}$, where $f(z) = \xi + (1-\xi)[1 - \exp(-z^2/2h^2)]$. The propagation parameters are summarized in Table S8.

The injection spectrum is assumed to be a PL in rigidity, $q_{\rm bkg}(R) \propto (R/{\rm GV})^{-\alpha}$. In the energy range we are interested in, the single PL injection is adequate, although more complicated injection form is required to reproduce the data in a wider energy range[63]. The spectral indices for different species differ slightly from each other, as given in Table S8. The spatial distribution is assumed to follow the Galactic SNR distribution[64], but with parameters slightly tuned based on γ-ray data[65]. The predicted secondary flux from the background CRs is consistent with the data[13, 17] for rigidity below $\sim$ TV, as can be seen in Figure S3. To better compare with the low-energy AMS-02 data, a force-field solar modulation with potential of 650 MV has been applied[66]. There might also be contribution from secondary interactions occurring around the sources given those particles may get trapped for some time[67, 68] (see, however, ref.[69] for a pessimistic opinion).

For the nearby source, we assume an instantaneous injection at time t and location $\mathbf{r}$. We assume the nearby source is Geminga-like[40], which has $r = 250$ pc and $t = 3.4 \times 10^5$ yr[70, 71]. Note that the distance and age of the nearby source are different from those of ref.[5], in which a ~ 2 Myr old nearby source with ~ 200 pc distance was assumed. The main difference is that, in ref.[5], the nearby source dominates the fluxes and anisotropies in the $1 - 100$ TeV band, while in our case, the contribution to the fluxes from the nearby source is sub-dominant and the anisotropies are jointly contributed by both components. The injection spectrum is assumed to be an exponential cutoff power-law (ECPL) form, $q_{\rm src} \propto (R/{\rm GV})^{-\beta} \exp(-R/R_c)$. The propagated flux at Earth can be obtained via the Green's function as, $\psi(r,t,R) = \frac{q_{\rm src}}{(\sqrt{2\pi}\sigma)^3} \exp\left(-\frac{r^2}{2\sigma^2}\right)$, where $\sigma(R,t) = [2D_{\rm disk}(R)t]^{1/2}$ is the effective diffusion length within time t. The slow diffusion coefficient $D_{\rm disk}$ is adopted. We find that for $\beta = 1.9$ and $R_c = 30$ TV, the bump features of spectra can be reproduced,

TABLE S8: **Model parameters used to give the results shown in Figure 3.**

Parameter	Background + nearby source	Propagation
r_h (kpc)	20.0	20.0
z_h (kpc)	5.0	5.0
D_0 (10^{28} cm^2 s^{-1})	2.42	2.06
δ_1	0.48	0.53
δ_2	0.20	0.13
$R_{\rm br}$ (GV)	300	700
δ_3	...	0.55
$R_{\rm br,2}$ (TV)	...	15
ξ	0.1	0.1
h (kpc)	0.45	0.45
$\alpha_{\rm p}$	2.48	2.36
$\alpha_{\rm he}$	2.38	2.28
$\alpha_{\rm c}$	2.40	2.30
$\alpha_{\rm o}$	2.42	2.32
$\alpha_{\rm fe}$	2.44	2.34
$N^a_{\rm p}$	6.60×10^2	6.98×10^2
$N^a_{\rm he}$	8.91×10^1	9.65×10^1
$N^a_{\rm c}$	1.07	1.12
$N^a_{\rm o}$	1.00	1.00
$N^a_{\rm fe}$	6.00×10^{-2}	5.80×10^{-2}
t (yr)	3.4×10^5	...
r (kpc)	0.25	...
β	1.90	...
R_c (TV)	30	...
$q^b_{\rm p}$	1.20×10^2	...
$q^b_{\rm he}$	3.80×10^1	...
$q^b_{\rm c}$	1.32	...
$q^b_{\rm o}$	1.00	...
$q^b_{\rm fe}$	0.14	...
Modulation potential (MV)	650	650

Notes. [a]Relative (background) source normalization parameters at 1 TV normalized to that of oxygen. [b]Relative normalizations of the nearby source component at 1 TV normalized to that of oxygen.

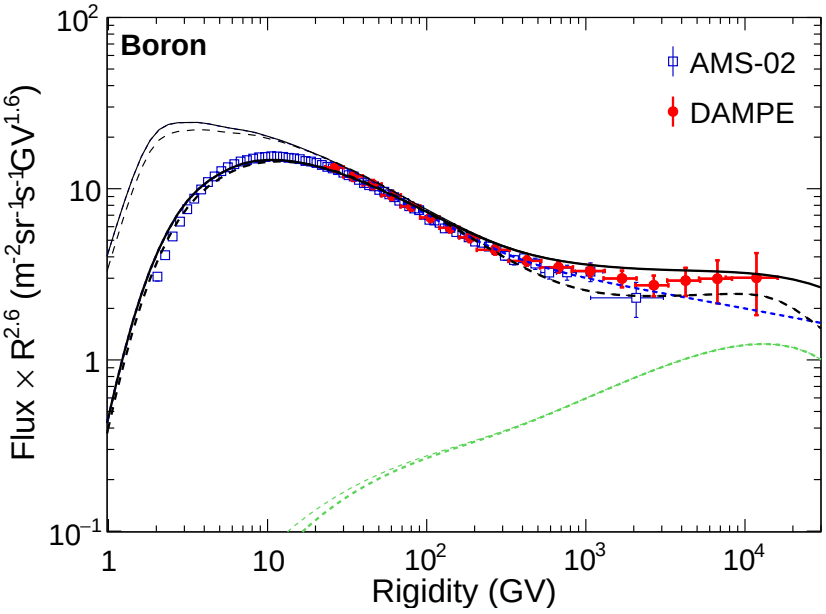

FIG. S3: **Rigidity spectra of boron weighted by $R^{2.6}$.** The solid lines show the results from the background plus nearby source model, with individual contributions from the two components being shown by dotted lines (blue for the background and green for the nearby source). The dashed lines show the results from the propagation model. Thin lines correspond to the results in the local interstellar medium and thick lines are modulated fluxes with potential of 650 MV. The measurements of AMS-02[13] and DAMPE[17] are shown for comparison.

as shown in Figure 3. Here the proton and oxygen spectra are shown for illustration. The same solar modulation potential of 650 MV is adopted. The expected boron flux from CRs produced by the nearby source is calculated with the same Green's function method through an integration over the volume and time assuming a gas density of 1 hydrogen cm^{-3}, which is also shown in Figure S3. The grammage for CRs from the nearby source can be estimated as $X \sim 0.3$ g cm^{-2} for the assumed gas density and a propagation time of $\sim 2 \times 10^5$ yr. We find that the contribution from the nearby source is sub-dominant in the whole energy range. Adding such a component can nevertheless better reproduce the data at the highest rigidity part.

The dipole component of the large-scale anisotropies from the model can be obtained as $\Delta = 3|\nabla(D_{\rm disk}\psi)|/(c\psi)$. Since the gradients from the background sources and the nearby source are different, a vector sum is necessary. We assume that the Galactic coordinate

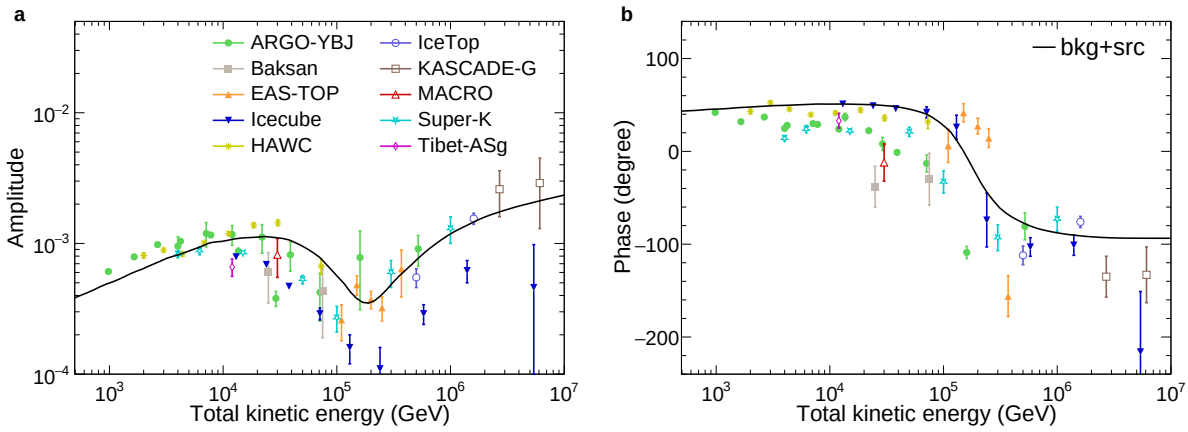

FIG. S4: **Dipole anisotropies of CRs.** Panel **a** shows the amplitudes of the dipole anisotropies, and panel **b** shows the phases. The solid lines show the predictions from the background plus nearby source model. The measurements are from: ARGO-YBJ[77], Baksan[78], EAS-TOP[79], HAWC[80], IceCube[81], IceTop[81], KASCADE-Grande[82], MACRO[83], Super-K[84], Tibet-ASγ[85].

of the nearby source is $(l, b) = (165°, -17°)$, which is close to but not exactly at the anti-Galactic-center direction. The location of the source in the sky is consistent with the fitting results obtained in ref.[40]. The resulting amplitude and phase (the right ascension of the maximum CR intensity) are shown in Figure S4., which reproduce properly the measurements. Particularly, at high energies (above a few hundred TeV), the anisotropy is dominated by the background which has a phase of $\sim -90°$ (Galactic center). At low energies, the anisitropy is in turn dominated by the nearby source, and a phase flip exists. There is also wide discussion about the effect of regulating the propagation of CRs by the local magnetic field[44, 72, 73]. The anisotropic diffusion in the directions perpendicular or parallel to the magnetic field would result in a projection of the CR flow onto the direction of the magnetic field[6, 73, 74]. In such a case, the original direction of the CR source becomes less correlated with the observed anisotropy direction, and the constraint on the location of the source is relaxed. In addition, it has been shown by the joint observation of HAWC and IceCube that there is a sharp division between excesses and deficits of the large-scale anisotropies, and there are also high-order anisotropies beyond the dipole[75]. More detailed studies are necessary to fully understand these observational facts of Galactic CRs.

The relative abundances (normalized to O = 1) of the measured CR fluxes at $R = 0.1$ TV

where the background sources dominate and $R = 10$ TV where the nearby source contributes a considerable fraction are shown in S5. The solar system abundances are also shown for reference[76]. One can see that heavier nuclei become more abundant at $R = 10$ TV than those at $R = 0.1$ TV, indicating that the nearby source tends to have higher metallicity than the background sources.

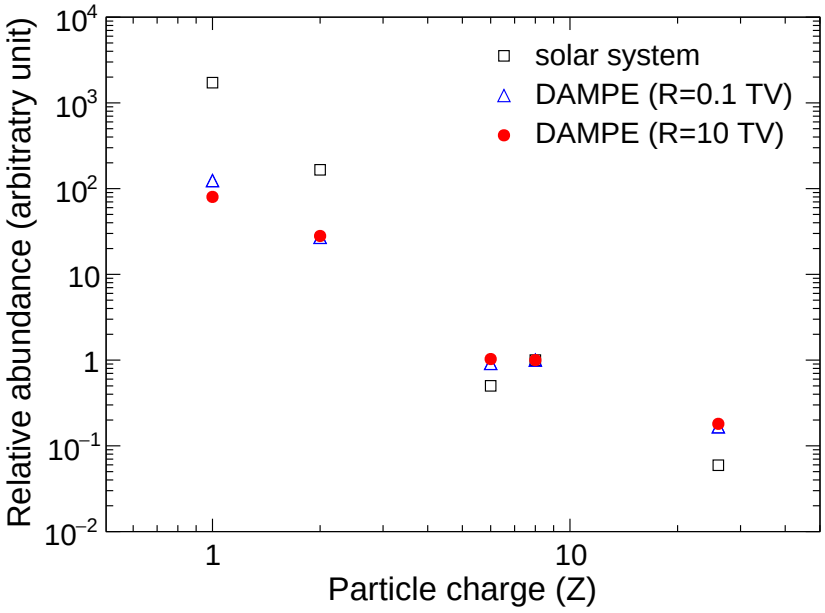

FIG. S5: **Relative abundances (normalized to oxygen) of the measurements.** Blue triangles show the results at 0.1 TV, red dots show those at 10 TV, and black squares show the solar system abundances[76].

(II) The propagation model. The other scenario is to ascribe the spectral breaks to a propagation effect. Two breaks of the diffusion coefficient are required to give the hardenings and subsequent softenings of the spectra. Physically this may be due to the self-generated turbulence with nonlinear Landau and ion-neutral damping of magnetohydrodynamic (MHD) waves by CRs, as proposed in ref.[8]. Here we empirically approximate the equivalent effect as a change of the rigidity dependence of the diffusion coefficient as

$$D(R) = \beta D_0 (R/\mathrm{GV})^{\delta_1} [1 + (R/R_{\mathrm{br}})^2]^{(\delta_2-\delta_1)/2} [1 + (R/R_{\mathrm{br},2})^5]^{(\delta_3-\delta_2)/5}. \quad (7)$$

Since the softening features are sharper than the hardening features in general, we assume different smoothness parameters of the breaks. Note that we also assume a two-halo propagation model, with the spatial dependence of the diffusion coefficient being the same as

above. The injection spectrum is again assumed to be a single PL form. The model parameters can be found in Table S8. The results for the secondary boron spectrum and primary proton and oxygen spectra are shown in Figure S3 and Figure 3 by dashed lines. While the spectral features can also be reproduced by the propagation model, whether the observed complicated behaviors of the large-scale anisotropies can be explained need further studies.

[46] Ambrosi, G. *et al.* The on-orbit calibration of DArk Matter Particle Explorer. *Astropart. Phys.* **106**, 18–34 (2019). 1907.02173.

[47] Zhao, C. *et al.* The study of fluorescence response to energy deposition in the BGO calorimeter of DAMPE. *Nucl. Instrum. Meth. A* **1029**, 166453 (2022).

[48] Zang, J. *et al.* Determination of the absolute energy scale of the DAMPE calorimeter with the geomagnetic rigidity cutoff method. *Astropart. Phys.* **173**, 103149 (2025). 2510.03854.

[49] Agostinelli, S. *et al.* GEANT4 - A Simulation Toolkit. *Nucl. Instrum. Meth. A* **506**, 250–303 (2003).

[50] Tykhonov, A. *et al.* TeV-PeV hadronic simulations with DAMPE. *Proc. Sci.* **ICRC2019**, 143 (2021).

[51] Chen, Z.-F. *et al.* BGO quenching effect on spectral measurements of cosmic-ray nuclei in DAMPE experiment. *Nucl. Instrum. Meth. A* **1055**, 168470 (2023). 2307.12629.

[52] Böhlen, T. T. *et al.* The FLUKA Code: Developments and Challenges for High Energy and Medical Applications. *Nucl. Data Sheets* **120**, 211–214 (2014).

[53] Smart, D. F. & Shea, M. A. A review of geomagnetic cutoff rigidities for earth-orbiting spacecraft. *Adv. Space Res.* **36**, 2012–2020 (2005).

[54] Tykhonov, A. *et al.* A deep learning method for the trajectory reconstruction of cosmic rays with the DAMPE mission. *Astropart. Phys.* **146**, 102795 (2023). 2206.04532.

[55] Dong, T. *et al.* Charge measurement of cosmic ray nuclei with the plastic scintillator detector of DAMPE. *Astropart. Phys.* **105**, 31–36 (2019). 1810.10784.

[56] Ma, P.-X. *et al.* A method for aligning the plastic scintillator detector on DAMPE. *Res. Astron. Astrophys.* **19**, 082 (2019). 1808.05720.

[57] Yue, C. *et al.* Correction method for the readout saturation of the DAMPE calorimeter. *Nucl. Instrum. Meth. A* **984**, 164645 (2020). 2009.09438.

[58] Serpolla, A. *et al.* Machine-learning correction for the calorimeter saturation of cosmic-rays ions with the Dark Matter Particle Explorer: towards the PeV scale. *Nucl. Instrum. Meth. A* **1085**, 171306 (2026). 2507.06626.

[59] Abdollahi, S. *et al.* Cosmic-ray electron-positron spectrum from 7 GeV to 2 TeV with the Fermi Large Area Telescope. *Phys. Rev. D* **95**, 082007 (2017). 1704.07195.

[60] Strong, A. W. & Moskalenko, I. V. Propagation of cosmic-ray nucleons in the galaxy. *Astrophys. J.* **509**, 212–228 (1998). astro-ph/9807150.

[61] Abeysekara, A. U. *et al.* Extended gamma-ray sources around pulsars constrain the origin of the positron flux at Earth. *Science* **358**, 911–914 (2017). 1711.06223.

[62] Aharonian, F. *et al.* Extended Very-High-Energy Gamma-Ray Emission Surrounding PSR J0622+3749 Observed by LHAASO-KM2A. *Phys. Rev. Lett.* **126**, 241103 (2021). 2106.09396.

[63] Boschini, M. J. *et al.* Inference of the Local Interstellar Spectra of Cosmic-Ray Nuclei $Z \leq 28$ with the GalProp-HelMod Framework. *Astrophys. J. Suppl.* **250**, 27 (2020). 2006.01337.

[64] Case, G. L. & Bhattacharya, D. A new sigma-d relation and its application to the galactic supernova remnant distribution. *Astrophys. J.* **504**, 761 (1998). astro-ph/9807162.

[65] Trotta, R. *et al.* Constraints on cosmic-ray propagation models from a global Bayesian analysis. *Astrophys. J.* **729**, 106 (2011). 1011.0037.

[66] Gleeson, L. J. & Axford, W. I. Solar Modulation of Galactic Cosmic Rays. *Astrophys. J.* **154**, 1011 (1968).

[67] Sun, D.-X., Zhang, P.-P., Yuan, Q. *et al.* Multimessenger observations support cosmic ray interactions surrounding acceleration sources. *Phys. Rev. D* **110**, 103039 (2024). 2307.02372.

[68] Yang, R. & Aharonian, F. Confinement of relativistic particles in the vicinity of accelerators: A key for understanding the anomalies in secondary cosmic rays. *Phys. Rev. D* **111**, 083040 (2025). 2410.22199.

[69] Recchia, S. *et al.* Grammage of cosmic rays in the proximity of supernova remnants embedded in a partially ionized medium. *Astron. Astrophys.* **660**, A57 (2022). 2106.04948.

[70] Smith, V. V., Cunha, K. & Plez, B. Is Geminga a runaway member of the Orion association? *Astron. Astrophys.* **281**, L41–L44 (1994).

[71] Manchester, R. N., Hobbs, G. B., Teoh, A. & Hobbs, M. The Australia Telescope National Facility pulsar catalogue. *Astron. J.* **129**, 1993 (2005). astro-ph/0412641.

[72] Battaner, E., Castellano, J. & Masip, M. Galactic magnetic fields and the large-scale anisotropy at MILAGRO. *Astrophys. J. Lett.* **703**, L90–L93 (2009). 0907.2889.

[73] Schwadron, N. A. *et al.* Global Anisotropies in TeV Cosmic Rays Related to the Sun's Local Galactic Environment from IBEX. *Science* **343**, 1245026 (2014).

[74] Liu, W., Lin, S.-j., Hu, H.-b., Guo, Y.-q. & Li, A.-f. Two Numerical Methods for the 3D Anisotropic Propagation of Galactic Cosmic Rays. *Astrophys. J.* **892**, 6 (2020). 1909.02908.

[75] Abeysekara, A. U. *et al.* All-Sky Measurement of the Anisotropy of Cosmic Rays at 10 TeV and Mapping of the Local Interstellar Magnetic Field. *Astrophys. J.* **871**, 96 (2019). 1812.05682.

[76] Lodders, K. Solar System Abundances and Condensation Temperatures of the Elements. *Astrophys. J.* **591**, 1220–1247 (2003).

[77] Bartoli, B. *et al.* Galactic Cosmic-Ray Anisotropy in the Northern Hemisphere from the ARGO-YBJ Experiment during 2008–2012. *Astrophys. J.* **861**, 93 (2018). 1805.08980.

[78] Alekseenko, V. V. *et al.* 10-100 TeV cosmic ray anisotropy measured at Baksan EAS 'Carpet' array. *Nucl. Phys. B Proc. Suppl.* **196**, 179–182 (2009). 0902.2967.

[79] Aglietta, M. *et al.* Evolution of the cosmic ray anisotropy above 10ˆ14 eV. *Astrophys. J. Lett.* **692**, L130–L133 (2009). 0901.2740.

[80] Abeysekara, A. U. *et al.* Observation of Anisotropy of TeV Cosmic Rays with Two Years of HAWC. *Astrophys. J.* **865**, 57 (2018). 1805.01847.

[81] Aartsen, M. G. *et al.* Anisotropy in Cosmic-ray Arrival Directions in the Southern Hemisphere Based on six Years of Data From the Icecube Detector. *Astrophys. J.* **826**, 220 (2016). 1603.01227.

[82] Chiavassa, A. *et al.* A study of the first harmonic of the large scale anisotropies with the KASCADE-Grande experiment. In *34th International Cosmic Ray Conference (ICRC2015)*, vol. 34 of *Int. Cosmic Ray Conf.*, 281 (2015).

[83] Ambrosio, M. *et al.* The Search for the sidereal and solar diurnal modulations in the total MACRO muon data set. *Phys. Rev. D* **67**, 042002 (2003). astro-ph/0211119.

[84] Guillian, G. *et al.* Observation of the anisotropy of 10-TeV primary cosmic ray nuclei flux with the super-kamiokande-I detector. *Phys. Rev. D* **75**, 062003 (2007). astro-ph/0508468.

[85] Amenomori, M. Northern sky Galactic Cosmic Ray anisotropy between 10-1000 TeV with the Tibet Air Shower Array. *Astrophys. J.* **836**, 153 (2017). 1701.07144.